PNAS RESEARCH ARTICLE | BIOPHYSICS AND COMPUTATIONAL BIOLOGY

Mechanism of RanGTP priming H2A-H2B release from Kap114 in an atypical RanGTP•Kap114•H2A-H2B complex

Jenny Jiou[a], Joy M. Shaffer[b], Natalia E. Bernades[a], Ho Yee Joyce Fung[a], Juliana Kikumoto Dias[b], Sheena D'Arcy[b], and Yuh Min Chook[a,1]

Edited by Tom Rapoport, Harvard University, Boston, MA; received January 20, 2023; accepted June 8, 2023

Previously, we showed that the nuclear import receptor Importin-9 wraps around the H2A-H2B core to chaperone and transport it from the cytoplasm to the nucleus. However, unlike most nuclear import systems where RanGTP dissociates cargoes from their importins, RanGTP binds stably to the Importin-9•H2A-H2B complex, and formation of the ternary RanGTP•Importin-9•H2A-H2B complex facilitates H2A-H2B release to the assembling nucleosome. It was unclear how RanGTP and the cargo H2A-H2B can bind simultaneously to an importin, and how interactions of the three components position H2A-H2B for release. Here, we show cryo-EM structures of Importin-9•RanGTP and of its yeast homolog Kap114, including Kap114•RanGTP, Kap114•H2A-H2B, and RanGTP•Kap114•H2A-H2B, to explain how the conserved Kap114 binds H2A-H2B and RanGTP simultaneously and how the GTPase primes histone transfer to the nucleosome. In the ternary complex, RanGTP binds to the N-terminal repeats of Kap114 in the same manner as in the Kap114/Importin-9•RanGTP complex, and H2A-H2B binds via its acidic patch to the Kap114 C-terminal repeats much like in the Kap114/Importin-9•H2A-H2B complex. Ran binds to a different conformation of Kap114 in the ternary RanGTP•Kap114•H2A-H2B complex. Here, Kap114 no longer contacts the H2A-H2B surface proximal to the H2A docking domain that drives nucleosome assembly, positioning it for transfer to the assembling nucleosome or to dedicated H2A-H2B chaperones in the nucleus.

nuclear import | histones | chaperone | importin | nucleosome assembly

Significance

Histones and their chaperone networks are typically conserved in eukaryotes. The yeast importin Kap114 and its human homolog Importin-9 share low sequence identity, but both are primary nuclear import receptors for the core histone heterodimer H2A-H2B. Cryo-EM structures of Kap114•H2A-H2B, Kap114•RanGTP, and Importin-9•RanGTP complexes show homologous structure and function for Kap114 and Importin-9. In the nucleus, RanGTP binding to Kap114/Imp9•H2A-H2B does not release H2A-H2B, but RanGTP binds to form an atypical ternary complex. The structure of the ternary RanGTP•Kap114•H2A-H2B complex explains how the GTPase and cargo bind simultaneously to Kap114 and how the presence of Ran in the complex primes H2A-H2B transfer to assembling nucleosomes or to nuclear chaperones.

In the nucleus, core histones H2A, H2B, H3, and H4 organize DNA into nucleosomes as 147 base pairs of DNA wrapped around the $(H3\text{-}H4)_2$ tetramer and two H2A-H2B dimers (1). Core histones are synthesized in the cytoplasm and folded into heterodimers that are actively transported into the nucleus by nuclear import receptors (importins) of the Karyopherin-β family. Cellular studies in *Saccharomyces cerevisiae* (*Sc*) and proteomic analysis of human cells identified the primary importins for H2A-H2B to be *Sc*Kap114 and its human homolog Importin-9 (Imp9, also known as IPO9) (2, 3). It was previously suggested that negatively charged importins could act as chaperones for highly positively charged nucleic acid-binding proteins (such as core histones) in addition to transporting them into the nucleus (4). The crystal structure of Imp9 bound to H2A-H2B showed the spiral-shaped HEAT-repeat containing importin wrapping around the globular histone-fold domain of H2A-H2B (5). This mode of interaction occludes large surfaces on H2A-H2B that bind DNA and H3-H4 in the nucleosome (5). Imp9 thus acts as a histone chaperone that shields H2A-H2B from spurious interactions with nucleic acids and proteins while transporting it from the cytoplasm into the nucleus.

After the Kap114/Imp9•H2A-H2B complex is transported into the nucleus across the nuclear pore complex, H2A-H2B still needs to be delivered to assembling nucleosomes. Typically, importin–cargo complexes are dissociated by the guanosine triphosphate (GTP)-bound Ran GTPase in the nucleus (6–9). High concentration of RanGTP in the nucleus is maintained by chromatin-bound β propeller protein RCC1 (Regulator of Chromatin Condensation 1) which is a Ran Guanine nucleotide Exchange Factor (RanGEF) that catalyzes the exchange to RanGTP (10–13). RanGTP often binds importins with high affinity, releasing cargo into the nucleus (14–18). However, nuclear import of H2A-H2B by Imp9 was shown to be an exception to this Ran-mediated cargo release mechanism. RanGTP does not release H2A-H2B from Imp9; instead, RanGTP binds the Imp9•H2A-H2B complex to form a stable RanGTP•Imp9•H2A-H2B complex (5). Within this ternary complex, RanGTP binding modulates Imp9-H2A-H2B interactions to allow H2A-H2B-DNA interactions and to facilitate in vitro deposition of H2A-H2B onto an assembling nucleosome. Pemberton and colleagues also found a stable assembly containing Imp9 homolog Kap114, H2A-H2B, RanGTP, and the histone chaperone Nap1 in the yeast nucleus (19).

Author contributions: S.D. and Y.M.C. designed research; J.J., J.M.S., N.E.B., H.Y.J.F., and J.K.D. performed research; J.J., J.M.S., N.E.B., H.Y.J.F., S.D., and Y.M.C. analyzed data; and J.J., J.M.S., H.Y.J.F., S.D., and Y.M.C. wrote the paper.

The authors declare no competing interest.

This article is a PNAS Direct Submission.

[1]To whom correspondence may be addressed. Email: YuhMin.Chook@utsouthwestern.edu.

This article contains supporting information online at https://www.pnas.org/lookup/suppl/doi:10.1073/pnas.2301199120/-/DCSupplemental.

Published July 14, 2023.

It was unclear how Kap114/Imp9 binds H2A-H2B and RanGTP simultaneously as a ternary complex of Ran, importin, and cargo is atypical among nuclear import complexes. It was also not known how RanGTP-binding changes Kap114/Imp9-H2A-H2B interactions within the ternary complex to facilitate in vitro nucleosome assembly. We solved cryogenic-electron microscopy (cryo-EM) structures of binary complexes Imp9•RanGTP, Kap114•RanGTP, and Kap114•H2A-H2B, which collectively show conservation of H2A-H2B and RanGTP recognition by Imp9 and its yeast homolog Kap114. Comparison of the H2A-H2B- versus Ran-bound binary complexes shows conformational changes at the N-terminal HEAT repeats of the importins, although there are few overlaps in the importin residues that bind H2A-H2B and RanGTP. The C-terminal HEAT repeats of the importins make extensive interactions with H2A-H2B but make no contact with RanGTP and are thus flexible in the importin•Ran structures. Most importantly, we solved the structure of the RanGTP•Kap114•H2A-H2B ternary complex, which shows that Kap114 binds H2A-H2B differently when RanGTP is also bound to the importin. The Kap114 C-terminal HEAT repeats maintain extensive contacts with the nucleosomal DNA and H3-H4-binding surfaces of H2A-H2B, but the Kap114 N-terminal HEAT repeats no longer contact the remaining nucleosomal DNA-binding surface of H2A-H2B. The exposed H2A-H2B surface allows interactions with DNA, facilitating transfer of H2A-H2B to the assembling nucleosome or to H2A-H2B chaperones in the nucleus.

Results

Interactions of Kap114 with H2A-H2B and RanGTP. We used pull-down binding assays, electrophoretic mobility shift assays (EMSAs), and analytical ultracentrifugation sedimentation analysis (AUC) to characterize Kap114 binding to H2A-H2B and RanGTP. Consistent with their homologous sequences, architectures, and functions, both Kap114 and Imp9 bind to H2A-H2B with subnanomolar affinities (*SI Appendix*, Fig. S1 *A–D*). Like all importins, they also both bind very tightly to RanGTP (K_Ds < 1nM) (*SI Appendix*, Fig. S1*E*). Pull-down binding assays show that immobilized maltose-binding protein (MBP)-Kap114 fusion bound H2A-H2B and RanGTP simultaneously; RanGTP does not cause displacement of H2A-H2B from Kap114 (Fig. 1*A*, controls in *SI Appendix*, Figs. S1*F* and S2*A*). EMSAs further show that Kap114 bound 1:1 to H2A-H2B

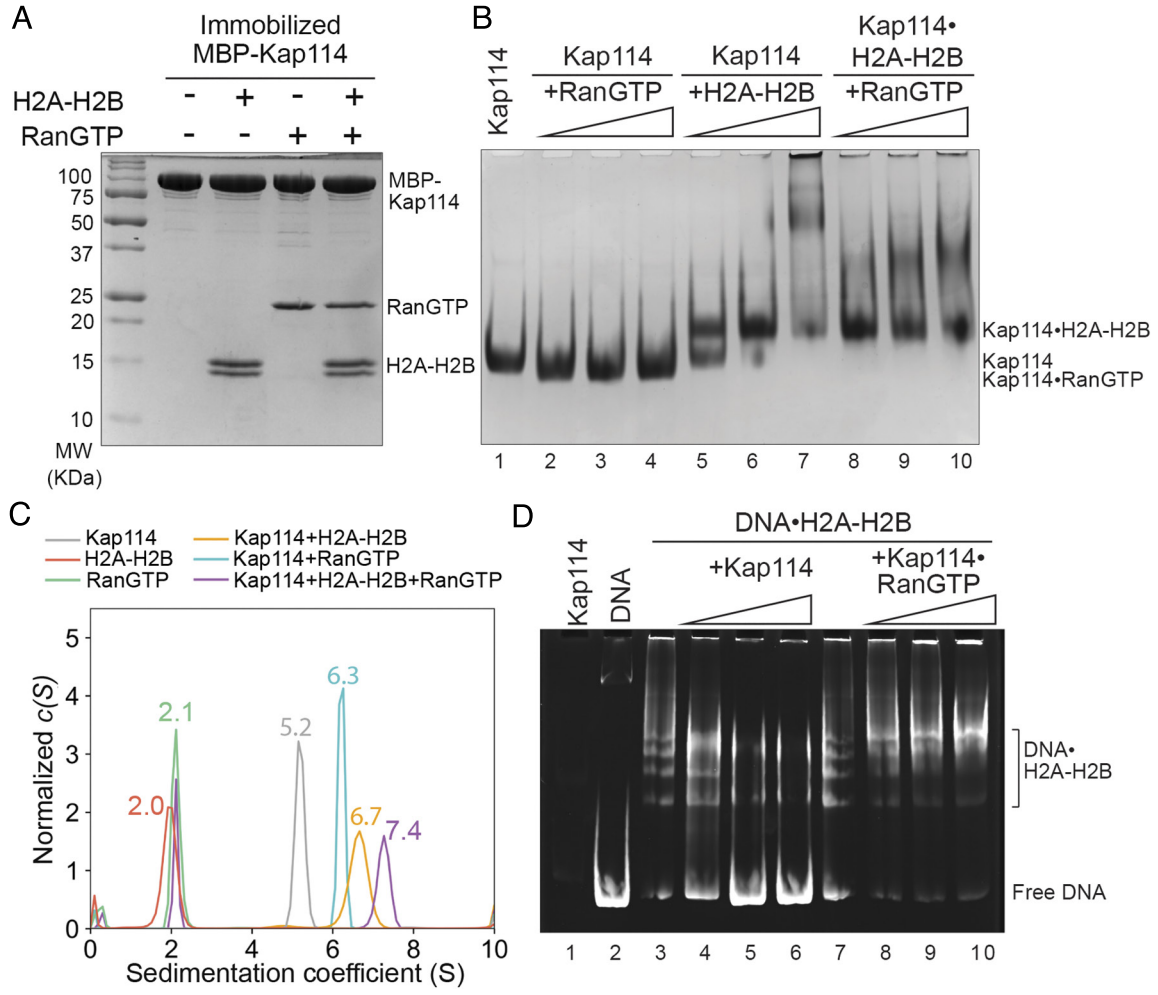

Fig. 1. Kap114 binding to H2A-H2B and RanGTP. (*A*) Pull-down binding assay of MBP-Kap114 immobilized on amylose beads with H2A-H2B and RanGTP. After extensive washing, bound proteins were visualized by Coomassie-stained SDS-PAGE. Controls are in *SI Appendix*, Fig. S2*A*. (*B*) Constant Kap114 was titrated with 0.5, 1, or 1.5 molar ratio of RanGTP (lanes 2 to 4) or H2A-H2B (lanes 5 to 7). Constant Kap114•H2A-H2B was titrated with 0.5, 1, or 1.5 molar ratio of RanGTP (lanes 8 to 10). Protein was visualized by Coomassie-stained native PAGE. (*C*) AUC sedimentation profiles of Kap114 (gray), H2A-H2B (red), RanGTP (green), 1:1 molar ratio of Kap114:H2A-H2B (orange), 1:1 molar ratio of Kap114:RanGTP (blue), and 1:1:3 molar ratio of Kap114:H2A-H2B:RanGTP (purple). (*D*) DNA competition assay with Kap114 (lanes 4 to 6) titrated at 0.5, 1, or 1.5 molar equivalents of H2A-H2B (in a DNA•H2A-H2B 1:7 complex), while Kap114•RanGTP (1:1, lanes 8 to 10) is titrated at 0.25, 0.5, or 1.0 molar equivalents of H2A-H2B (in a DNA•H2A-H2B 1:7 complex). Native PAGE was visualized with ethidium bromide. Coomassie staining is shown in *SI Appendix*, Fig. S2*C*.

or RanGTP and verified formation of a ternary complex of RanGTP•Kap114•H2A-H2B (Fig. 1*B* and *SI Appendix*, Fig. S2*B*). This stable ternary complex sediments at 7.4 S, compared to binary Kap114•RanGTP and Kap114•H2A-H2B complexes that sediment at 6.3 S and 6.7 S, respectively (Fig. 1*C*). As a measure of histone chaperone activity of Kap114, we performed DNA competition with Kap114 or Imp9 in the presence and absence of RanGTP (Fig. 1*D* and *SI Appendix*, Fig. S2 *C* and *D*). Both Imp9 and Kap114 bound H2A-H2B and released DNA from DNA•H2A-H2B while Imp9•RanGTP and Kap114•RanGTP did not (Fig. 1*D*, compare lanes 4 to 6 and 8 to 10 of *SI Appendix*, Fig. S2*D*). These results are consistent with Padavannil et al. where the presence of RanGTP changes Kap114/Imp9-H2A-H2B chaperoning ability (5). Kap114 and Imp9 are thus similar in having histone chaperone activity, in forming a ternary complex with RanGTP and H2A-H2B, and in RanGTP modulating importin–histone interactions within the ternary complex.

Structures of Binary Complexes Imp9•RanGTP, Kap114•RanGTP, and Kap114•H2A-H2B. We solved cryo-EM structures of the following binary complexes: Kap114•H2A-H2B (3.2 Å resolution), Kap114•RanGTP (3.5 Å resolution), and Imp9•RanGTP (3.7 Å resolution) (Fig. 2 *A* and *B* and *SI Appendix*, Figs. S1*B*, S3, and S4 and Tables S1 and S2). Imp9 and *Sc*Kap114 are 21.2% identical in sequence and share all key structural features, including 20 HEAT repeats (h1-h20, each containing antiparallel helices a and b) and three long loops (the h8 loop, the h18-h19 loop, and the acidic h19 loop) (*SI Appendix*, Fig. S5). Structures of Imp9 and Kap114 bound to H2A-H2B or to RanGTP are very similar.

When bound to H2A-H2B, Kap114 adopts a compact, superhelical architecture that is similar to Imp9 bound to H2A-H2B (Fig. 2*A* and *SI Appendix*, Fig. S6*A*). The Kap114 superhelix wraps around the H2A-H2B core using interactions conserved with Imp9 (*SI Appendix*, Figs. S5, S6*A*, and S7). The C-terminal ends of h3-h5 b helices, the loops that follow these helices and helix h2b, the loops of h17 and h18 repeats, the C-terminal end of the h19a helix, and the long h18-h19 loop all contact H2A-H2B. Sequence comparison of Kap114 and Imp9 reveals the greatest identity in the C-terminal HEAT repeats (27.3% identity aligning 319 residues of h16-h20); the h18-h19 loop is especially conserved. The N-terminal HEAT repeats (20.8% sequence identity aligning 240 residues of h1-h5) and the central HEAT repeats (17.9% identity aligning 549 residues of h6-h15) are also conserved (*SI Appendix*, Fig. S5). This sequence conservation is consistent with similar H2A-H2B binding by Kap114 and Imp9 at both their C- and N-terminal HEAT repeats (detail interactions in *SI Appendix*, Fig. S7).

RanGTP-bound structures of Kap114 and Imp9 are also very similar and are like the many previously reported importin•Ran structures (Fig. 2*B* and *SI Appendix*, Figs. S6–S8) (15, 20–26). Kap114 and Imp9 primarily use the b helices of h1-h4 to bind switch 1, switch 2, and helix α3 of RanGTP. Other interactions

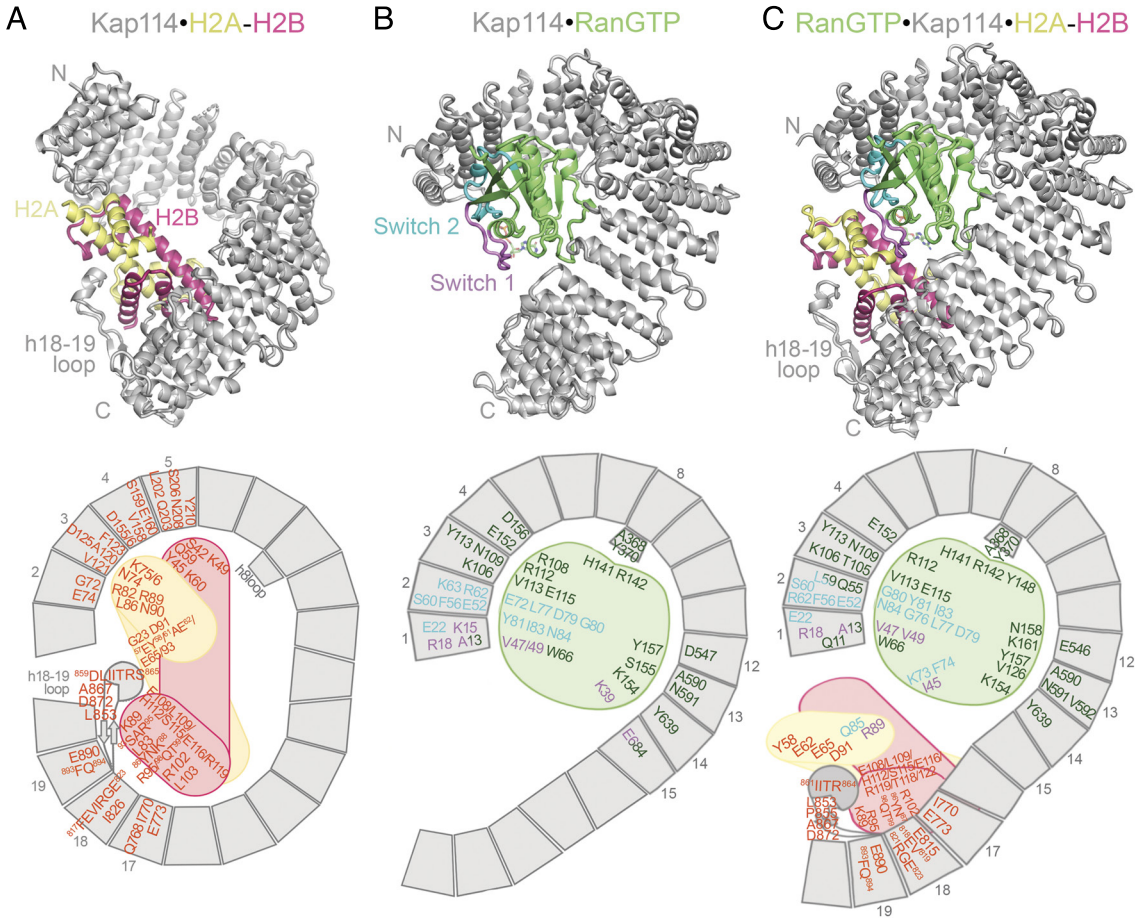

Fig. 2. Cryo-EM structures of Kap114•H2A-H2B, Kap114•RanGTP, and RanGTP•Kap114•H2A-H2B. (*A*) Cartoon representation of Kap114(gray)•H2A(yellow)-H2B(red) and a schematic showing all residues that participate in Kap114-H2A-H2B contacts (<4Å, orange). (*B*) Cartoon representation of Kap114•RanGTP. Switch 1 (violet), switch 2 (cyan), and GTP (sticks colored by atom) of RanGTP (green) are shown. A schematic shows residues participating in Kap114-RanGTP contacts colored as in the RanGTP structure. (*C*) Cartoon representation of RanGTP•Kap114•H2A-H2B with a schematic showing residues in Kap114-H2A-H2B and -RanGTP contacts, colored as in (*A*) and (*B*).

involve the extended h8 loops and h12-15 of the importins contacting helix α4 and switch 1 of RanGTP, respectively (detailed interactions in *SI Appendix*, Fig. S8). The C-terminal repeats of Kap114 (h16-h20) make no contact with RanGTP, consistent with three similarly-represented classes of Kap114•RanGTP cryo-EM particles that differ in the orientations of their C-terminal repeats (*SI Appendix*, Fig. S4*A*); only the highest resolution class 1 structure is determined and shown in Fig. 2*B* and *SI Appendix*, Fig. S4*B*. The flexible C-terminal repeats of Kap114 are also consistent with the lack of density for the likely very flexible h16-h20 of Imp9•RanGTP (*SI Appendix*, Fig. S3*C*).

Comparison of the Kap114•H2A-H2B and Kap114•RanGTP structures shows minimal overlap between residues that contact H2A-H2B *versus* RanGTP (*SI Appendix*, Fig. S5). However, the importin conformations, especially at the N-terminal regions, are quite different when bound to the two ligands (Fig. 2 *A* and *B*). The RanGTP-bound Kap114 superhelix is wider and has a shorter pitch than the H2A-H2B-bound one (*SI Appendix*, Fig. S9*A*). Alignments of HEAT repeats between the Kap114•H2A-H2B and Kap114•RanGTP structures reveal rigid body regions and hinges between them that describe the conformational differences (*SI Appendix*, Fig. S9*B*). Repeats h5-h13 are similar in the two structures (rmsd = 0.515 Å for 378 of 430 Cα atoms aligned), suggesting that this is a rigid body block. Meanwhile, high rmsds when aligning consecutive repeats suggest that h4-h5, h13-h14, and h16-h17 are hinges about which groups of HEAT repeats rotate (detailed analysis in *SI Appendix*, Fig. S9). These groups of repeats are 1) h1-h4 that contact H2A-H2B and RanGTP, 2) the invariant h5-h13 core, and 3) the h17-h20 repeats that make no contact with RanGTP and are very flexible in Kap114•RanGTP but make extensive contacts with H2A-H2B. The hinges at h4-h5 facilitate movement of the N-terminal repeats (h1-h4) relative to the central core repeats (h5-h13), while the h13-h14 and h16-h17 hinges facilitate movement of the C-terminal repeats (h17-h20) relative to the central core repeats (Fig. 2*C* and *SI Appendix*, Fig. S9*B*). Similar features of conformational change are observed for Imp9•H2A-H2B and Imp9•RanGTP (*SI Appendix*, Fig. S9*C*).

Structure of the RanGTP•Kap114•H2A-H2B Ternary Complex. It was unclear from the binary structures how the ternary complex is arranged when Kap114 binds RanGTP and H2A-H2B simultaneously. We assembled the RanGTP•Kap114•H2A-H2B complex for structure determination by cryo-EM. The data collected produced three classes of ternary complexes that differ in the orientations of Kap114 repeats h16-h20 (*SI Appendix*, Fig. S2*A*). We solved the structure of the most highly populated class 3, as it also has the highest local resolution for the C-terminal portion of Kap114 and the bound H2A-H2B (Fig. 2*C* and *SI Appendix*, Fig. S10*C*). The structure of this most open/fanned-out conformation of the RanGTP•Kap114•H2A-H2B complex was determined to 3.3 Å resolution (Fig. 2*C* and *SI Appendix*, Figs. S10 *B* and *C* and Table S1).

The RanGTP•Kap114•H2A-H2B structure (Fig. 2*C*) shows the N-terminal half of the Kap114 superhelix (composed of h1-h15) binding RanGTP by adopting the same conformation (rmsd = 0.625 Å, 587 of 701 Cα atoms aligned) and making the same interactions with the GTPase as the binary Kap114•RanGTP structure (Figs. 2 *B* and *C* and 3 *A* and *B* and *SI Appendix*, Fig. S5). Residues in the Kap114 h1-h4 repeats that contacted H2A-H2B in Kap114•H2A-H2B are still accessible in the ternary complex, but this region is now further away from the bound H2A-H2B and no longer contacts it (the shortest distance between H2A-H2B and the h2-3loop of Kap114 is ~5 Å) (Fig. 3 *C* and *D*). This newly exposed surface of H2A-H2B is also proximal to the H2A C-terminal docking domain and tail (residue 82-119) that interacts with H3-H4 in the nucleosome (no density is present for the H2A C-terminal tail in either structure). The RanGTP•Kap114•H2A-H2B structure shows a few contacts between the RanGTP switches and H2A, but the lack of H2A-H2B side chain densities, consistent with local resolution of 4.5 Å for H2A-H2B as shown in *SI Appendix*, Fig. S10*B*, suggests that these Ran–histone interactions are transient (Fig. 3*C*).

The region C-terminal of h16 in Kap114 does not contact RanGTP but adopts the same conformation and maintains the same extensive contacts with H2A-H2B as in the Kap114/Imp9•H2A-H2B structures (Fig. 3*E* and *SI Appendix*, Fig. S7). The C-terminal region of Kap114, with H2A-H2B bound, adopts different orientations relative to the N-terminal half of the importin in the different cryo-EM classes of particles (Fig. 2*D* and *SI Appendix*, Fig. S10*A*). Movements of the histone-bound Kap114 C-terminal region likely occur about the hinge at h16-h17, similar to Kap114•RanTP (*SI Appendix*, Figs. S9 and S10*A*). The maps for the 3 classes of both Kap114•RanGTP and RanGTP•Kap114•H2A-H2B are similar with only small differences in the angle/pitch of the C-terminal region (*SI Appendix*, Fig. S10*A*).

The GTPase in RanGTP•Kap114•H2A-H2B Primes Transfer of H2A-H2B to Nucleosomes. We performed nucleosome assembly assays where we titrated H2A-H2B and Kap114 in the presence or absence of RanGTP into tetrasomes (Fig. 4*A* and *SI Appendix*, Fig. S11). Like Imp9, Kap114 facilitated H2A-H2B deposition, forming a nucleosome, only in the presence of RanGTP (Fig. 4*A* and *SI Appendix*, Fig. S11). Without RanGTP, Kap114/Imp9 inhibited H2A-H2B deposition. The RanGTP-induced release of the contacts between H2A-H2B and the N-terminal HEAT repeats of Kap114/Imp9 clearly makes H2A-H2B more available to form nucleosomal interactions with DNA and H3-H4. These results are consistent with our structural data.

We compared the location of nucleosomal interfaces of H2A-H2B to Kap114•H2A-H2B and RanGTP•Kap114•H2A-H2B structures to understand how RanGTP facilitates H2A-H2B release to the assembling nucleosome (Fig. 4 *B* and *C*). In Kap114•H2A-H2B, a large portion of the nucleosomal DNA-binding surface of H2A-H2B is obstructed by the N- and C-terminal regions of Kap114 (Fig. 4*C*). The region of H2A-H2B that interfaces with H3-H4 through a four-helix bundle in the nucleosomes is also covered by the C-terminal region of Kap114 (Fig. 4*C*). This extensive occlusion in the binary Kap114/Imp9•H2A-H2B complex explains the poor ability to release H2A-H2B to DNA (Fig. 1*D*) or tetrasomes (Fig. 4*A* and S11A and B). Occlusion of H2A-H2B is altered in the ternary RanGTP•Kap114•H2A-H2B structure. Although the Kap114 C-terminal repeats still cover part of the nucleosomal DNA- and H3-H4-binding surfaces of H2A-H2B, the Kap114 N-terminal repeats no longer engage the remaining nucleosomal DNA-binding surface of H2A-H2B. This exposure of a long stretch of DNA-binding residues proximal to the H2A docking domain makes H2A-H2B more available for potential capture by DNA (Fig. 1*D*) or the assembling nucleosome (Fig. 4*C*). These structural observations are consistent with the nucleosome assembly assays where the RanGTP•Kap114/Imp9•H2A-H2B complex effectively deposits H2A-H2B onto assembling nucleosomes (Fig. 4*A* and *SI Appendix*, Fig. S11).

Discussion

Kap114 behaves like Imp9 in all our structural, biophysical, and biochemical analyses. Their structures bound to H2A-H2B or RanGTP are very similar with only minor differences, such as no

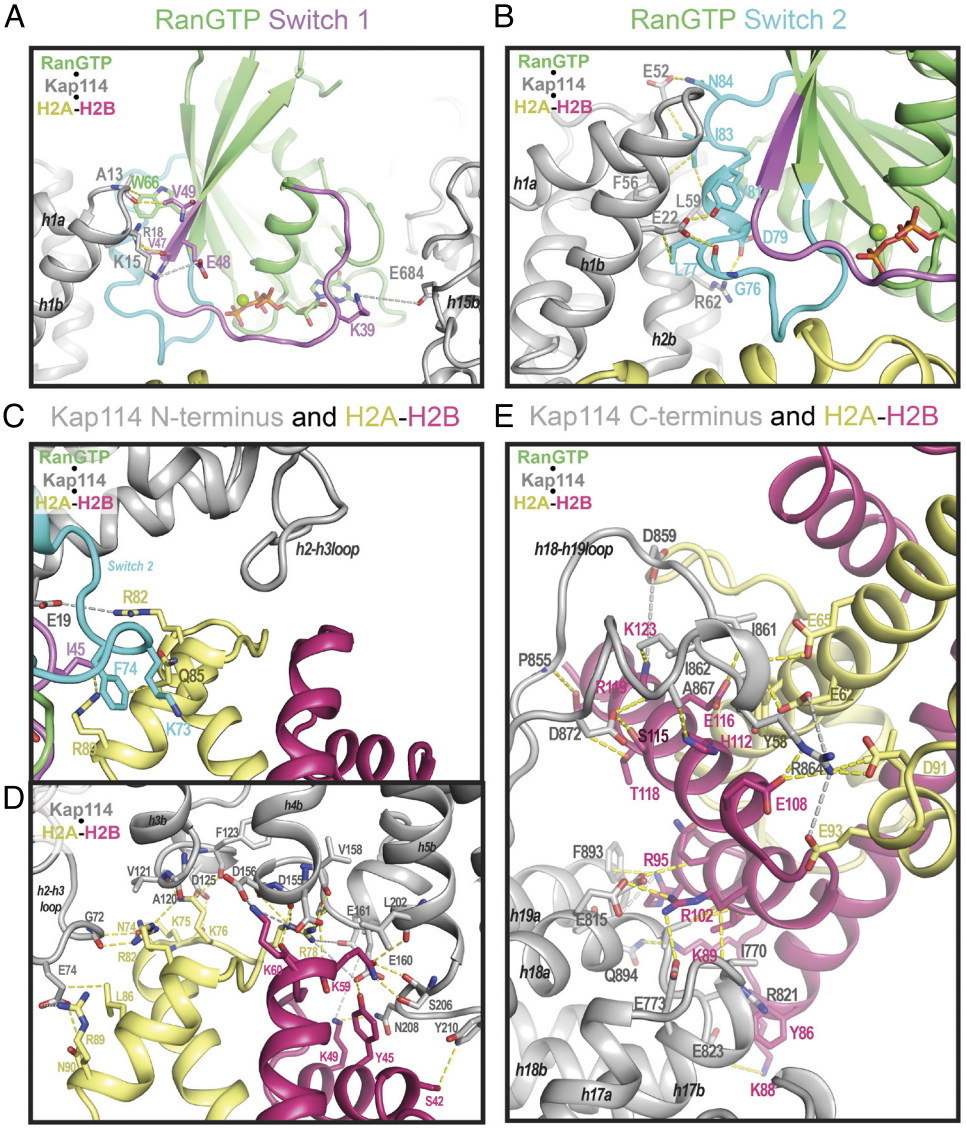

Fig. 3. Interactions of the ternary RanGTP•Kap114•H2A-H2B complex. (*A* and *B*) Select interactions of Kap114 with RanGTP switch 1 (*A*) and switch 2 (*B*). (*C*) Interactions between Kap114 N-terminal repeats with RanGTP and H2A-H2B. (*D*) Similar view and orientation as in (*C*) for the binary Kap114•H2A-H2B structure. (*E*) The Kap114 C-terminal repeats in the ternary RanGTP•Kap114•H2A-H2B structure. In all panels, Kap114 is gray, RanGTP is green (switch 1 violet and switch 2 cyan), H2A is yellow, and H2B is red. Dashed lines represent interactions <4 Å (yellow) and long-range electrostatic interactions <8 Å (gray).

interaction between Kap114 and the H2B N-terminal tail compared to three to five tail residues seen bound to Imp9 (5). The lack of H2B tail contacts with Kap114 is consistent with previous findings that the histone tails are not important for Imp9 binding and that the removal of the histone tails does not affect their nuclear import (5, 27). Both Imp9 and Kap114 occlude the nucleosomal DNA-binding regions of H2A-H2B with their N-terminal HEAT repeats and the nucleosomal DNA- and histone-binding sites with their C-terminal HEAT repeats. Such extensive interfaces render Imp9 and Kap114 effective H2A-H2B chaperones that compete interactions between H2A-H2B and DNA.

However, the very high affinity and extensive importin–histone interactions could make it difficult to release H2A-H2B in the nucleus. Indeed, unlike other import cargos that are easily dissociated from their importins by RanGTP, the GTPase cannot release H2A-H2B from Kap114 or Imp9 except in the presence of assembling nucleosomes. The stable RanGTP•Kap114•H2A-H2B complex allows Kap114 to continue to chaperone H2A-H2B in the nucleus, consistent with the generally accepted notion that there is no free H2A-H2B in the cell (28, 29). H2A-H2B release becomes targeted as conformational changes in RanGTP•Kap114•H2A-H2B release contacts between H2A-H2B and the N-terminal HEAT repeats of Kap114 to make H2A-H2B available for interactions with nucleosomal DNA and H3-H4. These findings are validated and extended to Imp9 by solution HDX analysis (30).

Although we have provided a structural understanding for how RanGTP primes the release of H2A-H2B from Kap114/Imp9 to assembling nucleosomes in vitro, many questions remain about this process in cells. First, it is unclear whether H2A-H2B is released directly from the Ran-bound Kap114/Imp9 to the assembling nucleosome or if the histone is released to dedicated nuclear chaperones of H2A-H2B, which then transfer the histone onto the nucleosome (Fig. 4*C*). It is also possible that histone chaperones and DNA/tetrasome work in concert to release H2A-H2B from Kap114. Potentially relevant H2A-H2B chaperones in the nucleus include Nap1, nucleoplasmin, and FACT (FAcilitates Chromatin Transcription, reviewed in ref. 31). Nap1 is a likely candidate to assist in histone release as it is also imported by Kap114 in yeast

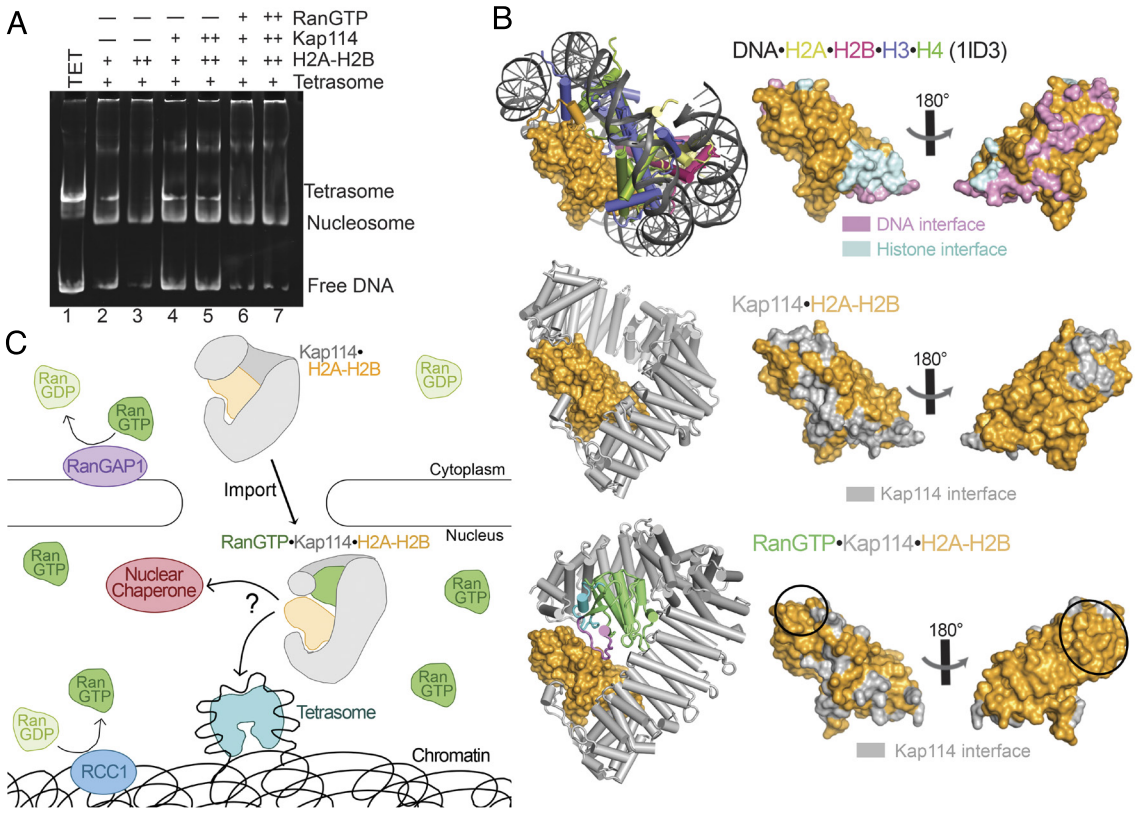

Fig. 4. The mechanism of RanGTP facilitating H2A-H2B release. (*A*) Nucleosome assembly assay where either H2A-H2B, Kap114•H2A-H2B or RanGTP•Kap114•H2A-H2B is titrated in molar equivalents of 2.0 and 3.0 to tetrasome (TET; 1.25 μM). Ethidium bromide–stained gel is shown. The same gel is Coomassie-stained in *SI Appendix*, Fig. S11*A*. (*B*) Top left, nucleosome (PDB 1ID3; DNA in dark gray and H2A-H2B-H3-H4 in yellow-red-blue-green) showing a single copy of H2A-H2B in the orange surface. Top right, H2A-H2B is shown alone with its nucleosome DNA and histone interfaces in pink and cyan, respectively. The H2A-H2B on the left is in the same orientation as shown in the nucleosome. Middle and bottom panels, Kap114 interfaces (gray) in the Kap114•H2A-H2B or RanGTP•Kap114•H2A-H2B structures. The regions exposed upon RanGTP binding to Kap114•H2A-H2B are indicated by black circles. (*C*) A model to illustrate how Kap114 imports H2A-H2B into the nucleus. RanGTP binding (enriched in the nucleus due to chromatin-tethered RCC1 and cytoplasmic RanGAP1) in the stable RanGTP•Kap114•H2A-H2B complex exposes a surface of H2A-H2B that may facilitate direct interactions with DNA and deposition directly onto a tetrasome for nucleosome assembly or facilitate interactions with/hand-off to nuclear chaperones.

cells and was shown to bind Kap114 and H2A-H2B in the yeast nucleus (2, 19). Second, it is unclear whether additional factors beyond the obvious candidates—assembling nucleosome and/or nuclear H2A-H2B chaperones—are involved in releasing H2A-H2B from Kap114 in cells. Third, sumoylation of Kap114 was reported to improve the ability of RanGTP to release cargoes Sua7 (also known as TFIIb) and TBP (32). The sumoylation site, mapped to residue K909, is in the long disordered acidic h19 loop that is not modeled in any of our Kap114 structures. Deletion of the h19 loop in Imp9 did not significantly affect H2A-H2B binding (5); it remains unclear whether sumoylation regulates RanGTP-mediated release of H2A-H2B from Kap114/Imp9. Finally, we showed that RanGTP•Kap114/Imp9 cannot disassemble H2A-H2B from nucleosomes, but it is not known whether nuclear Kap114/Imp9 in the presence of RanGTP may chaperone H2A-H2B after it is removed from the nucleosome by remodelers during replication, transcription, or DNA repair (33, 34). Kap114 shuttles between the nucleus and the cytoplasm. At steady state, it is distributed across the two compartments, and there is a substantial pool of the importin in the nucleus (35). It is unclear whether Kap114 has additional functions in the nucleus beyond dropping off H2A-H2B for nucleosome assembly.

We have revealed how Kap114 chaperones H2A-H2B in the cytoplasm and in the nucleus, the latter in the form of the RanGTP•Kap114•H2A-H2B complex. Our previous study of Imp9 binding to H2A-H2B and solution HDX analysis of Imp9 show that this importin uses the same mechanism (30). This knowledge is the foundation to understand how additional molecular players contribute to H2A-H2B cytoplasmic processing and deposition into the nucleosome.

Methods

Constructs, Protein Expression, and Purification. *Sc*Kap114 was cloned into two modified vectors: pGEX-4T3 (GE Healthcare) and pmalE (New England BioLabs). The pGEX-43T was modified to have a Tobacco Etch Virus (TEV) protease cleavage site inserted between the GST tag and Kap114. The pmalE was modified to have a His-tag at the N terminus of MBP and a TEV cleavage site after the MBP.

The plasmid was transformed into BL21-Gold(DE3) and plated on Luria Broth (LB) agar with ampicillin for selection. Kap114 was expressed using 6 L of LB media and induced with 0.5 mM isopropyl β-D-1-thiogalactopyranoside (IPTG) for 16 h at 20 °C. Cells were spun at 4,000 rpm with a Sorvall BP8 (Thermo Fisher) equipped with a HAEMAFlex 6 rotor for 30 min at 4 °C and resuspended in lysis buffer (20 mM Tris–HCl pH 7.5, 1 M NaCl, 15% (v/v) glycerol, 2 mM dithiothreitol (DTT for GST-Kap114) or 2 mM β-mercaptoethanol (BME for His_6MBP-Kap114), cOmplete ethylenediaminetetraacetic acid (EDTA)-free Protease Inhibitor Cocktail (Roche Applied Science). Cells were lysed with an Emulsiflex-C5 cell homogenizer (Avestin) and centrifuged in an Avanti J-26 XPI with a JA-25.50 rotor (Beckman Coulter) at 20,000 relative centrifugal force (RCF) for 1 h at 4 °C. The supernatant was decanted into a gravity, affinity column. GST-Kap114 was purified with Glutathione Sepharose 4B (Cytiva), and the GST tag was cleaved on column using TEV protease. His_6MBP-Kap114 was purified with Ni^{2+}-NTA Agarose (Qiagen). Once eluted, the Kap114 or His_6MBP-Kap114 was further purified by ion-exchange chromatography using HiTrap Q HP (Cytiva), and gel filtration chromatography using Superdex 200 16/600 (Cytiva). Proteins

were stored in the gel filtration buffer containing 20 mM Tris–HCl pH 7.5, 150 mM NaCl, and 2 mM DTT.

Human Imp9 and *Sc*Ran (Gsp1 residues 1-179 with Q71L, which stabilize the GTP-bound conformation, destabilize the very different guanosine diphosphate (GDP)-bound conformation, and abolish the GTPase activity) were expressed and purified as previously described (5, 36). To ensure Ran is fully loaded with GTP, EDTA stripping and GTP loading were performed (36). *Sc*/*Xenopus laevis* (*Xl*) histones were obtained from The Histone Source and refolded according to the established protocol (1). Using established protocols (1), 147 bp DNA was purified and assembled into tetrasomes.

mNeonGreen was subcloned from pL0M-S-mNeonGreen-EC18153 into pET28a along with GSP1(1-179, Q71L). pL0M-S-mNeonGreen-EC18153 was a gift from Julian Hibberd (RRID:Addgene 137075). mNeonGreen-GSP1 was expressed in Rosetta(DE3)pLysS cells using 2 L of LB media with kanamycin and chloramphenicol for selection. The cells were induced with 0.25 mM IPTG for 12 h at 18 °C. Protein was purified as for GSP1. H2A-K119C was labeled with XFD488 (ATT Bioquest) and prepared according to the manufacturer's protocol.

Pull-Down Binding Assays. Pull-down binding assays were performed by immobilizing purified His_6MBP or His_6MBP-Kap114 on amylose resin (New England BioLabs). Resin was stored in binding assay (BA) buffer containing 20 mM Tris–HCl pH 7.5, 150 mM NaCl, 10% (v/v) glycerol, and 2 mM DTT forming a 50% amylose resin and 50% BA buffer slurry. One hundred microliters of slurry with a total solution volume of 50 µL BA buffer was brought up to a total solution volume of 100 µL with a final concentration of 10 µM His_6MBP or His_6MBP-Kap114, 50 µM *Sc*H2A-H2B, and/or 50 µM RanGTP. RanGTP was added after a 30-min preincubation period of the other components and equilibrated for another 30 min at room temperature. Amylose resin was pelleted at 16,000 RCF for 1 min at 4 °C using an Eppendorf Centrifuge 5415 R and washed three times with 600 µL of BA buffer stored at 4 °C with excess solution carefully aspirated. One hundred microliters of 2× Laemmli sample buffer was added, and BA samples were boiled for 5 min. Ten microliters of the sample was loaded onto a 12% SDS-PAGE gel. Gels were visualized using Coomassie stain.

EMSAs. For EMSAs with Imp9, one component was held constant at 10 µM, while the other was titrated. For EMSAs with Kap114, one component was held constant at 5 µM, while the other was titrated. Proteins were dialyzed into the same buffer overnight [20 mM HEPES (N-2-hydroxyethylpiperazine-N'-2-ethanesulfonic acid), pH 7.5, 150 mM NaCl, 2 mM MgAcetate, 2 mM Tris(2-carboxyethyl)phosphine hydrochloride (TCEP), and 10% (v/v) glycerol]. Samples were separated by 5% native PAGE. Gels were run for 100 min at 150 V at 4 °C in 0.5× TBE (40 mM Tris–HCl pH 8.4, 45 mM boric acid, and 1 mM EDTA). Gels were stained with Coomassie. The gel shown was one of ≥3 repeats.

Analytical Ultracentrifugation. Sedimentation velocity experiments were performed as described in Padavannil et al. (5). Individual proteins were dialyzed into analytical ultracentrifugation (AUC) buffer containing 20 mM Tris–HCl pH 7.5, 150 mM NaCl, 2 mM $MgCl_2$, and 2 mM TCEP. Five hundred microliters of the AUC sample was equilibrated overnight at 4 °C. The AUC sample chamber contained 400 µL of the following: 1) 3 µM Kap114, 2) 10 µM ScH2A-H2B, 3) 10 µM RanGTP, 4) 3 µM Kap114 + 3 µM H2A-H2B, 5) 3 µM Kap114 + 3 µM RanGTP, and 6) 3 µM Kap114 + 3 µM H2A-H2B + 10 µM RanGTP. Sedimentation coefficients were measured by monitoring absorbance at 280 nm in a Beckman-Coulter Optima XL-1 Analytical Ultracentrifuge. The Beckman data time stamps were corrected using REDATE (37). SEDNTERP was used to calculate the buffer density, buffer viscosity, and protein partial-specific volumes (38). Analysis by SEDFIT involves lamm equation modeling and was used to calculate sedimentation coefficient distributions c(S) where the regularization calculated a confidence level of 0.68 was used, time-independent noise elements were accounted for, and at a resolution of 100 (39). SEDFIT was also used to obtain the sedimentation coefficient by integration of c(S) and the frictional ratios by refining the fit of the model. The data were plotted using GUSSI (40).

DNA Competition Assays. Imp9, Kap114, Imp9•RanGTP, or Kap114•RanGTP were titrated at various molar equivalents of *Xl*H2A-H2B where H2A-H2B was in a 7:1 complex with 147 bp Widom 601 DNA (10.5 µM H2A-H2B and 1.5 µM DNA). Binary complexes were preassembled using equimolar Imp9 and RanGTP or Kap114 and RanGTP added together without further purification. Proteins were dialyzed in the same buffer overnight [20 mM HEPES, pH 7.5, 300 mM NaCl, 2 mM Mg acetate, 2 mM TCEP, and 10% (v/v) glycerol]. Samples were separated by 5% native PAGE. Gels were run for 75 min at 150 V at 4 °C in 0.5× TBE. Gels were stained with ethidium bromide and then Coomassie. The gel shown was one of ≥3 repeats.

Fluorescent Polarization. Fluorescence polarization (FP) assays were performed in a 384-well format as previously described (36). Kap114 and Imp9 were dialyzed overnight into 20 mM HEPES pH 7.5, 150 mM NaCl, 2 mM $MgCl_2$, 2 mM TCEP, and 10% (v/v) glycerol. Kap114 or Imp9 were serially diluted with buffer and mixed with ^{XFD488}H2A-H2B or mNeonGreen-RanGTP at indicated concentrations. Triplicate reactions were analyzed in black-bottom plates (Corning), and data were collected in a CLARIOstar plus plate reader (BMG Labtech) equipped with dichroic filter LP 504. Measurement was performed with top optics with an excitation range of 482-16 nm and emission range of 530-40 nm, 50 flashes per well with a 0.1-s settling time. Detector gain and focal height for the measurement were adjusted using well with ^{XFD488}H2A-H2B and the lowest concentration of Kap114 to target mP of 200 and kept constant for the rest of the measurements unless otherwise noted. Data were analyzed in PALMIST (41) and fitted with a 1:1 binding model, using the error-surface projection method to calculate the 95% CIs of the fitted data. Fitted data were exported and plotted in GUSSI.

Cryo-EM Sample Preparation. For Kap114•H2A-H2B and Kap114•RanGTP, individual proteins were buffer exchanged into cryo-EM buffer containing 20 mM Tris–HCl pH 7.5, 300 mM NaCl, 2 mM $MgCl_2$, and 1 mM TCEP and flash frozen at 8 mg/mL. Kap114•H2A-H2B and Kap114•RanGTP were made by mixing Kap114 with *Sc*H2A-H2B or RanGTP, resulting in a 1 Kap114 to 1.2 H2A-H2B or RanGTP molar ratio at 8 mg/mL. Kap114 complexes were diluted twofold with cryo-EM buffer plus NP-40 at a final concentration of 0.1% (w/v). Samples of Imp9•RanGTP were buffer exchanged into 50 mM Tris–HCl pH 7.5, 150 mM NaCl, and 0.1% (w/v) NP-40 at a final protein concentration of 3 mg/mL. Four microliters of Kap114•H2A-H2B/RanGTP or 3.5 µL of Imp9•RanGTP was applied to a 300-mesh copper grid (Quantifoil R1.2/1.3) that was glow-discharged using a PELCO easiGlow glow discharge apparatus for 30 mA/30 s on top of a metal grid holder (Ted Pella). The excess sample was blotted 3 s with 595 filter paper (Ted Pella, #47000-100) before plunge-freezing in a ThermoFisher Vitrobot System at 4 °C with 95% humidity.

RanGTP•Kap114•H2A-H2B was cross-linked on a Superdex 200 10/300 Increase column equilibrated with cryo-EM buffer. We injected 500 µL of 0.05% (w/v) glutaraldehyde with 3 mL of buffer followed by 500 µL of an equimolar mix of RanGTP, Kap114, and H2A-H2B. We collected 0.5 mL fractions. The ternary complex was concentrated to 8.6 mg/mL and was flash-frozen in liquid nitrogen. The complex was diluted twofold with cryoEM buffer plus Tween-20 [final concentration of 0.00125% (w/v)]. The grid was glow-discharged, blotted, and plunge-frozen in a similar manner as the binary complexes.

Cryo-EM Data Collection. Cryo-EM data for Kap114•H2A-H2B and Kap114•RanGTP were collected at the Pacific Northwest Cryo-EM Center on a Titan Krios at 300 kV with a Gatan K3 detector in correlated double sampling super-resolution mode at a magnification of 81,000× corresponding to a pixel size of 0.5295 Å. Each movie was recorded for a total of 58 frames over 3.475 s with an exposure rate of 15 electrons/pixel/s (total dose of 50 $e^-/Å^2$). Datasets were collected using SerialEM (42) software with a defocus range of −0.8 and −2.5 µm.

Cryo-EM data collection for Imp9•RanGTP and RanGTP•Kap114•H2A-H2B was performed at the UT Southwestern Cryo-Electron Microscopy Facility on a Titan Krios at 300 kV with a Gatan K3 detector in correlated double sampling super-resolution mode, with an energy filter of 20 eV slit width, at a magnification of 105,000× corresponding to a pixel size of 0.415 Å. Each movie was recorded for a total of 60 frames over 5.4 s with an exposure rate of 7.8 electrons/pixel/s (total dose of 52 $e^-/Å^2$). The datasets were collected using SerialEM with a defocus range of −0.9 and −2.4 µm.

Cryo-EM Data Processing. A total of 9,158 movies were collected for Kap114•H2A-H2B, and 5,744 movies were collected for Kap114•RanGTP. Both datasets were processed using cryoSPARC, using default settings for all jobs unless noted otherwise, (43) where they were first subjected to Patch Motion Correction (Kap114•H2A-H2B unbinned and Kap114•RanGTP binned twice) and Patch CTF Estimation. The Blob Picker was implemented on 50 micrographs to pick all possible particles with little bias, and this small set of particles was subjected to 2D

Classification to generate 2D templates where a subset of templates was used in Template Picker. A total of 7,006,373 particles were picked from the Kap114•H2A-H2B dataset, and 7,640,457 particles were picked from the Kap114•RanGTP dataset. After five rounds of 2D Classification for both datasets, 671,257 particles of Kap114•H2A-H2B and 953,500 particles of Kap114•RanGTP were selected. The Kap114•H2A-H2B particles were then sorted into four 3D classes, while the Kap114•RanGTP particles were sorted into six 3D classes using Ab-initio reconstruction followed by Heterogeneous Refinement. The particles from two Kap114•H2A-H2B 3D classes were combined to give 554,529 particles for Non-uniform Refinement, with preparticle defocus optimized in defocus refinement, which yielded a 3.21 Å resolution map. Three classes of Kap114•RanGTP– class 1 with 277,305 particles, class 2 with 258,006 particles, and class 3 with 259,220 particles–were individually subjected to Non-uniform Refinement, with pregroup CTF parameters optimized in global CTF refinement. We analyzed the local resolution at a 0.5 Fourier Shell Correlation (FSC) threshold and determined that class 1 was the best for model building.

A total of 4,767 movies were collected for the RanGTP•Kap114•H2A-H2B complex. This dataset was also processed using cryoSPARC. The movies were subjected to Patch Motion Correction (binned twice) and Patch CTF Estimation. Generation of templates was performed as for the binary complexes, and 3,401,608 particles were extracted from the Template Picks. After five rounds of 2D Classification, 604,835 particles were further processed into five Ab-Initio classes and five Heterogeneous Refinement classes. Two of the five classes contained the complex of interest and were subjected to another round of Ab-Initio and Heterogeneous Refinement which generated four new classes. Three classes from Heterogeneous Refinement were subjected to Non-uniform Refinement: class 1 with 3.50 Å resolution using 114,232 particles, class 2 with 3.49 Å resolution using 95,715 particles, and class 3 with 3.28 Å resolution using 134,915 particles. For reconstruction of the class 3 map, both per-particle defocus and per-group CTF parameters were refined. All maps had local resolution analyzed at a 0.5 FSC threshold, and class 3 was the best one for model building.

A total of 4,920 movies were collected for Imp9•RanGTP and processed using cryoSPARC. A ½ F-crop factor was applied during motion correction followed by patch CTF estimation. A small set of ~20 frames was used to generate the initial template for particle picking. A total of 2,474,170 particles were initially extracted from all the micrographs. The first round of 2D classification produced 904,566 particles that were subjected to another three rounds of 2D classification. 232,798 particles were included for Ab-Initio modeling followed by heterogeneous refinement. Non-uniform Refinement was carried out to generate the final 3.7 Å resolution map.

Cryo-EM Model Building, Refinement, and Analysis. The Kap114 proteins in both Kap114•H2A-H2B and Kap114•RanGTP structures were built using coordinates of unliganded Kap114 from the crystal structure PDB 6AHO (44). The *Sc*H2A-H2B in Kap114•H2A-H2B was built using *Xl*H2A-H2B coordinates from the Imp9•H2A-H2B crystal structure PDB 6N1Z (5) and the RanGTP in Kap114•RanGTP built using coordinates of canine Ran in Kap121•RanGTP crystal structure PDB 3W3Z (23). The Imp9•RanGTP structure was also built using coordinates from PDB 6N1Z and PDB 3W3Z. The RanGTP•Kap114•H2A-H2B complex used Kap114 h1-h15 and RanGTP from the Kap114•RanGTP model and Kap114 h16-h20 and H2A-H2B from Kap114•H2A-H2B. All the models were roughly docked into the map using UCSF Chimera (45) before subjected to real-space refinement with default settings of global minimization, rigid body, local grid search, Atomic Displacement Parameters (ADP or B-factors), and NQH flip refinement for 10 macrocycles, with secondary structure and Ramachandran restraints on Phenix (46). This is followed by manual rounds of rebuilding using Coot (47) and ISOLDE (48) on UCSF (University of California San Francisco) ChimeraX (49) and real-space refinement in Phenix (as described earlier but without rigid body refinement) until acceptable PHENIX validation parameters are achieved. Structure interfaces were analyzed using ENDscript 2.0 (50) with contacts cutoff of 4 Å. These contacts were then manually curated and mapped onto a multiple sequence alignment generated by MAFFT (51) and visualized by ESPript 3.0 (50). We used PyMOL version 2.5 for 3D structure analysis (52).

Nucleosome Assembly Assays. Tetrasomes containing *Xl*$(H3\text{-}H4)_2$ and 147 bp Widom 601 DNA were reconstituted as described in Dyer et al. (53). To monitor nucleosome assembly, tetrasomes were held constant at 1.25 μM, and H2A-H2B or preformed complexes of Imp9•H2A-H2B (1:1), RanGTP•Imp9•H2A-H2B (1:1:1), Kap114•H2A-H2B (1:1), or RanGTP•Kap114•H2A-H2B (1:1:1) were titrated at 2 and 3 molar equivalents. Proteins were dialyzed into the same buffer overnight (20 mM HEPES, pH 7.5, 150 mM NaCl, 2 mM Mg acetate, 2 mM TCEP, and 10% (v/v) glycerol). Samples were separated by 5% native PAGE. Gels were run for 75 min at 150 V at 4 °C in 0.5× TBE. Gels were stained with ethidium bromide and then Coomassie. The gel shown was one of ≥3 repeats.

Data, Materials, and Software Availability. Structure/CryoEM Maps data have been deposited in PDB/EMDB (8F0X, 8F19, 8F1E, and 8F7A/EMD-28788, 28782, 28796, and 28899) (54–57).

ACKNOWLEDGMENTS. We thank Abhilash Padavannil for the important biochemical studies that led to this work. A portion of this research was supported by NIH grant U24GM129547 and performed at the Pacific Northwest Center for Cryo-EM (PNCC) at Oregon Health & Science University and accessed through Environmental Molecular Sciences Laboratory (grid.436923.9), a DOE Office of Science User Facility sponsored by the Office of Biological and Environmental Research. We thank the Structural Biology Laboratory and the Cryo-EM Facility at University of Texas Southwestern Medical Center (UTSW), which are partially supported by grant RP170644 from the Cancer Prevention & Research Institute of Texas, for cryo-EM studies for their assistance with cryo-EM data collection. We thank Chad Brautigam and the Macromolecular Biophysics Resource at UTSW for training and use of their analytical ultracentrifuge. We also thank the Erzberger lab for the use of their equipment for fluorescence polarization experiments. We acknowledge The Histone Source at Colorado State University for generating the *Xl* and *Sc* histone H2A and H2B proteins used in this study. This work was funded by the National Institute of General Medical Sciences (NIGMS) of NIH under Awards R35GM141461 (Y.M.C.), R01GM069909 (Y.M.C.), R35GM133751 (S.D.), and T32GM008203 (J.J.), the Welch Foundation Grants I-1532 (Y.M.C.), AT-2059-20210327 (S.D.), and NSF MRI 2018188 (S.D.), support from the Alfred and Mabel Gilman Chair in Molecular Pharmacology, Eugene McDermott Scholar in Biomedical Research (Y.M.C.), Mary Kay International Postdoctoral Fellowship (N.E.B.), and the Gilman Special Opportunities Award (H.Y.J.F.).

Author affiliations: [a]Department of Pharmacology, University of Texas Southwestern Medical Center, Dallas, TX 75390; and [b]Department of Chemistry and Biochemistry, The University of Texas at Dallas, Richardson, TX 75080

1. K. Luger, A. W. Mader, R. K. Richmond, D. F. Sargent, T. J. Richmond, Crystal structure of the nucleosome core particle at 2.8 A resolution. *Nature* **389**, 251–260 (1997).
2. N. Mosammaparast *et al.*, Nuclear import of histone H2A and H2B is mediated by a network of karyopherins. *J. Cell Biol.* **153**, 251–262 (2001).
3. M. Kimura *et al.*, Extensive cargo identification reveals distinct biological roles of the 12 importin pathways. *Elife* **6**, e21184 (2017).
4. S. Jakel, J. M. Mingot, P. Schwarzmaier, E. Hartmann, D. Gorlich, Importins fulfil a dual function as nuclear import receptors and cytoplasmic chaperones for exposed basic domains. *EMBO J.* **21**, 377–386 (2002).
5. A. Padavannil *et al.*, Importin-9 wraps around the H2A–H2B core to act as nuclear importer and histone chaperone. *Elife* **8**, e43630 (2019).
6. D. Gorlich, N. Pante, U. Kutay, U. Aebi, F. R. Bischoff, Identification of different roles for RanGDP and RanGTP in nuclear protein import. *EMBO J.* **15**, 5584–5594 (1996).
7. K. Weis, Regulating access to the genome: Nucleocytoplasmic transport throughout the cell cycle. *Cell* **112**, 441–451 (2003).
8. S. R. Wente, M. P. Rout, The nuclear pore complex and nuclear transport. *Cold Spring Harb Perspect Biol.* **2**, a000562 (2010).
9. M. Soniat, Y. M. Chook, Nuclear localization signals for four distinct karyopherin-beta nuclear import systems. *Biochem. J.* **468**, 353–362 (2015).
10. M. E. Nemergut, C. A. Mizzen, T. Stukenberg, C. D. Allis, I. G. Macara, Chromatin docking and exchange activity enhancement of RCC1 by histones H2A and H2B. *Science* **292**, 1540–1543 (2001).
11. R. D. Makde, J. R. England, H. P. Yennawar, S. Tan, Structure of RCC1 chromatin factor bound to the nucleosome core particle. *Nature* **467**, 562–566 (2010).
12. F. R. Bischoff, H. Ponstingl, Mitotic regulator protein RCC1 is complexed with a nuclear ras-related polypeptide. *Proc. Natl. Acad. Sci. U.S.A.* **88**, 10830–10834 (1991).
13. L. Renault *et al.*, The 1.7 A crystal structure of the regulator of chromosome condensation (RCC1) reveals a seven-bladed propeller. *Nature* **392**, 97–101 (1998).
14. C. E. Wing, H. Y. J. Fung, Y. M. Chook, Karyopherin-mediated nucleocytoplasmic transport. *Nat. Rev. Mol. Cell Biol.* **23**, 307–328 (2022).

15. Y. M. Chook, G. Blobel, Structure of the nuclear transport complex karyopherin-beta2-Ran x GppNHp. *Nature* **399**, 230–237 (1999).
16. D. Gorlich, U. Kutay, Transport between the cell nucleus and the cytoplasm. *Annu. Rev. Cell Dev. Biol.* **15**, 607–660 (1999).
17. J. Bednenko, G. Cingolani, L. Gerace, Nucleocytoplasmic transport: Navigating the channel. *Traffic* **4**, 127–135 (2003).
18. A. Cook, F. Bono, M. Jinek, E. Conti, Structural biology of nucleocytoplasmic transport. *Annu. Rev. Biochem.* **76**, 647–671 (2007).
19. N. Mosammaparast, B. C. Del Rosario, L. F. Pemberton, Modulation of histone deposition by the karyopherin kap114. *Mol. Cell Biol.* **25**, 1764–1778 (2005).
20. I. R. Vetter, A. Arndt, U. Kutay, D. Gorlich, A. Wittinghofer, Structural view of the Ran-Importin beta interaction at 2.3 A resolution. *Cell* **97**, 635–646 (1999).
21. S. J. Lee, Y. Matsuura, S. M. Liu, M. Stewart, Structural basis for nuclear import complex dissociation by RanGTP. *Nature* **435**, 693–696 (2005).
22. M. Grunwald, F. Bono, Structure of Importin13-Ubc9 complex: Nuclear import and release of a key regulator of sumoylation. *EMBO J.* **30**, 427–438 (2011).
23. J. Kobayashi, Y. Matsuura, Structural basis for cell-cycle-dependent nuclear import mediated by the karyopherin Kap121p. *J. Mol. Biol.* **425**, 1852–1868 (2013).
24. G. N. Maertens *et al.*, Structural basis for nuclear import of splicing factors by human Transportin 3. *Proc. Natl. Acad. Sci. U.S.A.* **111**, 2728–2733 (2014).
25. V. G. Tsirkone *et al.*, Structure of transportin SR2, a karyopherin involved in human disease, in complex with Ran. *Acta Crystallogr. F Struct. Biol. Commun.* **70**, 723–729 (2014).
26. N. E. Bernardes, H. Y. J. Fung, Y. Li, Z. Chen, Y. M. Chook, Structure of IMPORTIN-4 bound to the H3-H4-ASF1 histone-histone chaperone complex. *Proc. Natl. Acad. Sci. U.S.A.* **119**, e2207177119 (2022).
27. C. Thiriet, J. J. Hayes, A novel labeling technique reveals a function for histone H2A/H2B dimer tail domains in chromatin assembly in vivo. *Genes Dev.* **15**, 2048–2053 (2001).
28. A. Gunjan, J. Paik, A. Verreault, The emergence of regulated histone proteolysis. *Curr. Opin. Genet Dev.* **16**, 112–118 (2006).
29. C. M. Hammond, C. B. Stromme, H. Huang, D. J. Patel, A. Groth, Histone chaperone networks shaping chromatin function. *Nat. Rev. Mol. Cell Biol.* **18**, 141–158 (2017).
30. J. M. Shaffer *et al.*, Molecular basis of RanGTP-activated release of Histones H2A–H2B from Importin-9. *Structure* (2023), https://doi.org/10.1101/2023.01.27.525896 (Accessed 28 January 2023).
31. Y. Huang, Y. Dai, Z. Zhou, Mechanistic and structural insights into histone H2A–H2B chaperone in chromatin regulation. *Biochem. J.* **477**, 3367–3386 (2020).
32. U. Rothenbusch, M. Sawatzki, Y. Chang, S. Caesar, G. Schlenstedt, Sumoylation regulates Kap114-mediated nuclear transport. *EMBO J.* **31**, 2461–2472 (2012).
33. K. M. Keck, L. F. Pemberton, Histone chaperones link histone nuclear import and chromatin assembly. *Biochim. Biophys. Acta* **1819**, 277–289 (2013).
34. N. Avvakumov, A. Nourani, J. Cote, Histone chaperones: Modulators of chromatin marks. *Mol. Cell* **41**, 502–514 (2011).
35. L. F. Pemberton, J. S. Rosenblum, G. Blobel, Nuclear import of the TATA-binding protein: Mediation by the karyopherin Kap114p and a possible mechanism for intranuclear targeting. *J. Cell Biol.* **145**, 1407–1417 (1999).
36. H. Y. J. Fung, Y. M. Chook, Binding affinity measurement of nuclear export signal peptides to their exporter CRM1. *Methods Mol. Biol.* **2502**, 245–256 (2022).
37. H. Zhao *et al.*, Recorded scan times can limit the accuracy of sedimentation coefficients in analytical ultracentrifugation. *Anal. Biochem.* **437**, 104–108 (2013).
38. T. M. S. Laue, B. Ridgeway, T. M. Pelletier, *"Computer-aided Interpretation of Sedimentation Data for Proteins" in Analytical Ultracentrifugation in Biochemistry and Polymer Science* (Royal Society of Chemistry, Cambridge, U.K., pp. 90–125. 1992).
39. P. Schuck, Size-distribution analysis of macromolecules by sedimentation velocity ultracentrifugation and lamm equation modeling. *Biophys. J.* **78**, 1606–1619 (2000).
40. C. A. Brautigam, Calculations and publication-quality illustrations for analytical ultracentrifugation data. *Methods Enzymol.* **562**, 109–133 (2015).
41. T. H. Scheuermann, S. B. Padrick, K. H. Gardner, C. A. Brautigam, On the acquisition and analysis of microscale thermophoresis data. *Anal Biochem.* **496**, 79–93 (2016).
42. D. N. Mastronarde, Automated electron microscope tomography using robust prediction of specimen movements. *J. Struct. Biol.* **152**, 36–51 (2005).
43. A. Punjani, J. L. Rubinstein, D. J. Fleet, M. A. Brubaker, cryoSPARC: Algorithms for rapid unsupervised cryo-EM structure determination. *Nat. Methods* **14**, 290-+ (2017).
44. C. C. Liao *et al.*, Karyopherin Kap114p-mediated trans-repression controls ribosomal gene expression under saline stress. *EMBO Rep.* **21**, e48324 (2020).
45. E. F. Pettersen *et al.*, UCSF chimera - A visualization system for exploratory research and analysis. *J. Comput. Chem.* **25**, 1605–1612 (2004).
46. P. D. Adams *et al.*, PHENIX: A comprehensive Python-based system for macromolecular structure solution. *Acta Crystallogr. D* **66**, 213–221 (2010).
47. P. Emsley, New tools for ligand refinement and validation in coot and CCP4. *Acta Crystallogr. A* **74**, A390 (2018).
48. T. I. Croll, ISOLDE: A physically realistic environment for model building into low-resolution electron-density maps. *Acta Crystallogr. D Struct. Biol.* **74**, 519–530 (2018).
49. E. F. Pettersen *et al.*, UCSF ChimeraX: Structure visualization for researchers, educators, and developers. *Protein Sci.* **30**, 70–82 (2021).
50. X. Robert, P. Gouet, Deciphering key features in protein structures with the new ENDscript server. *Nucleic Acids Res.* **42**, W320–324 (2014).
51. K. Katoh, D. M. Standley, MAFFT multiple sequence alignment software version 7: Improvements in performance and usability. *Mol. Biol. Evol.* **30**, 772–780 (2013).
52. W. L. DeLano, "PyMOL molecular viewer: Updates and refinements" in Abstracts of Papers of the American Chemical Society (American Chemical Society, 2009), **vol. 238**.
53. P. N. Dyer *et al.*, Reconstitution of nucleosome core particles from recombinant histones and DNA. *Methods Enzymol.* **375**, 23–44 (2004).
54. J. Jiou, Y. M. Chook, Cryo-EM structure of Kap114 bound to H2A-H2B. Protein Data Bank. https://doi.org/10.2210/pdb8f0x/pdb. Deposited 8 November 2022.
55. J. Jiou, Y. M. Chook, Cryo-EM structure of Kap114 bound to Gsp1 (RanGTP). Protein Data Bank. https://doi.org/10.2210/pdb8f19/pdb. Deposited 8 November 2022.
56. J. Jiou, Y. M. Chook, Cryo-EM structure of Kap114 bound to Gsp1 (RanGTP) and H2A-H2B. Protein Data Bank. https://doi.org/10.2210/pdb8f1e/pdb. Deposited 8 November 2022.
57. N. Bernardes, Y. M. Chook, Cryo-EM structure of Importin-9 bound to RanGTP. Protein Data Bank. https://doi.org/10.2210/pdb8f7a/pdb. Deposited 18 November 2022.